Supporting Information

Characterization of Synthesized Gibbsite NPTs

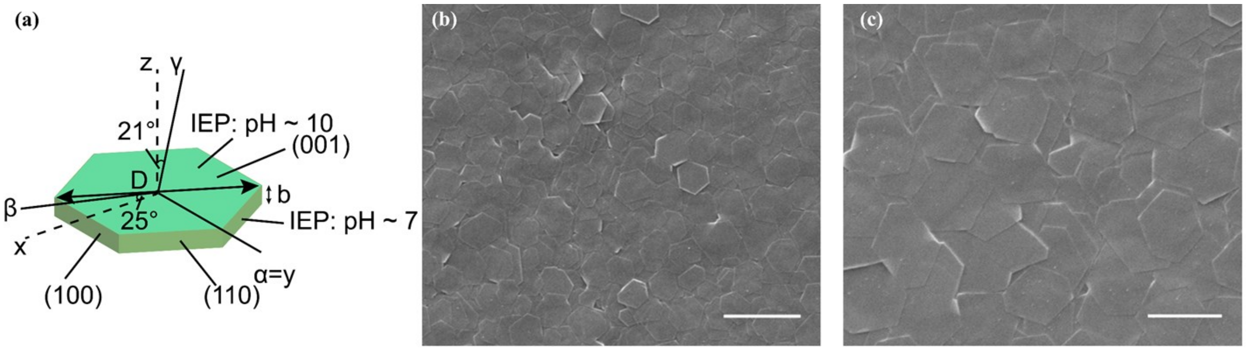

Figure S1. (a) Crystallographic axes and isoelectric points of hexagonal gibbsite NPTs.[1,2] SEM images of gibbsite NPTs after (b) one-time synthesis (c) one seeded-growth step. All scale bars are 500 nm.

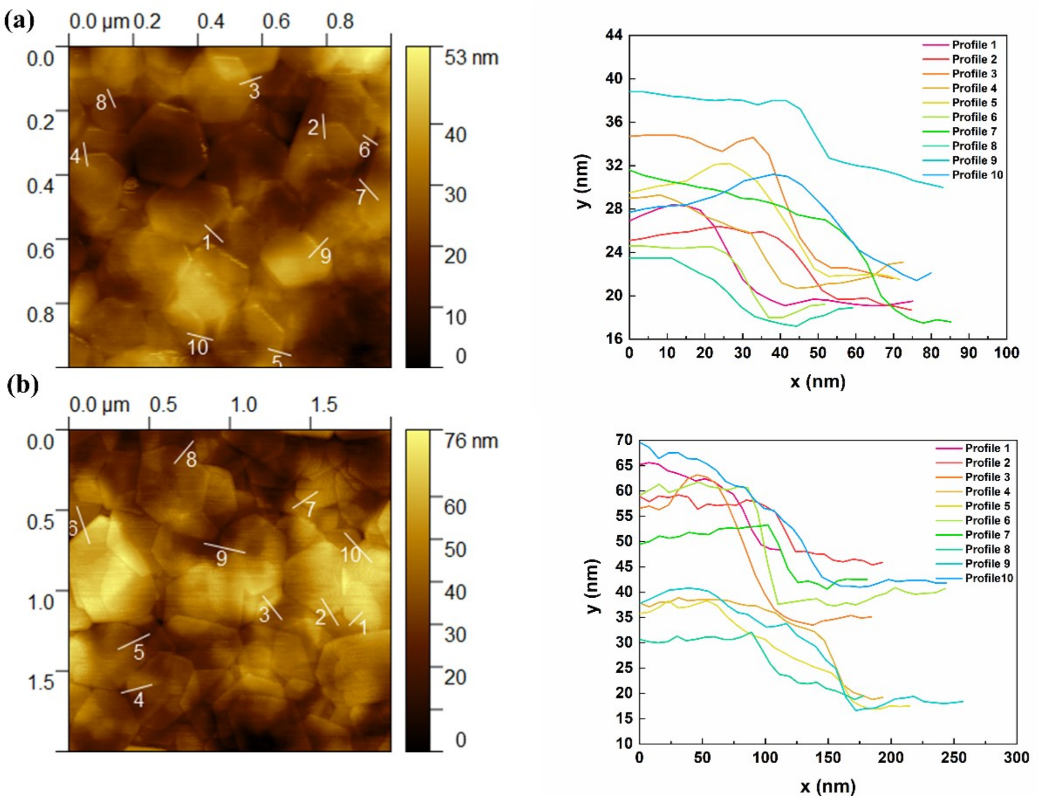

Figure S2. AFM images and corresponding line scan profiles of gibbsite NPTs after (a) one-time synthesis (c) one seeded-growth step.

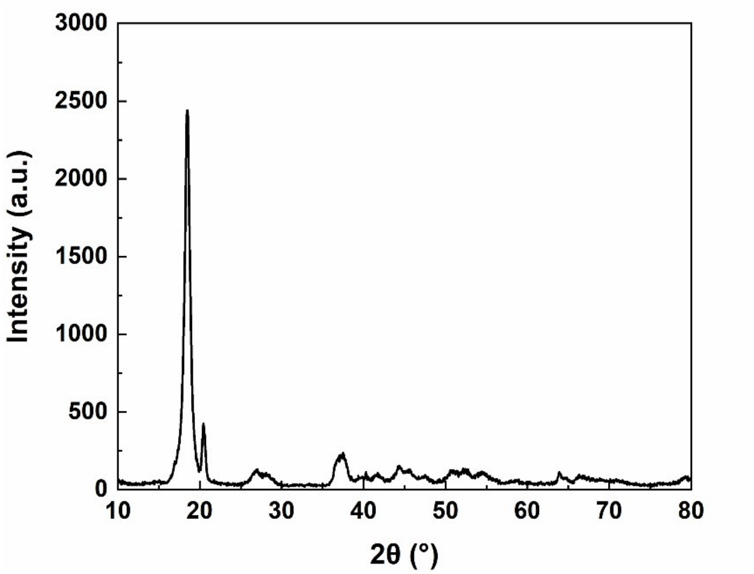

Figure S3. X-ray powder diffraction pattern of synthesized gibbsite NPTs.

Flow Coating of Gibbsite NPTs

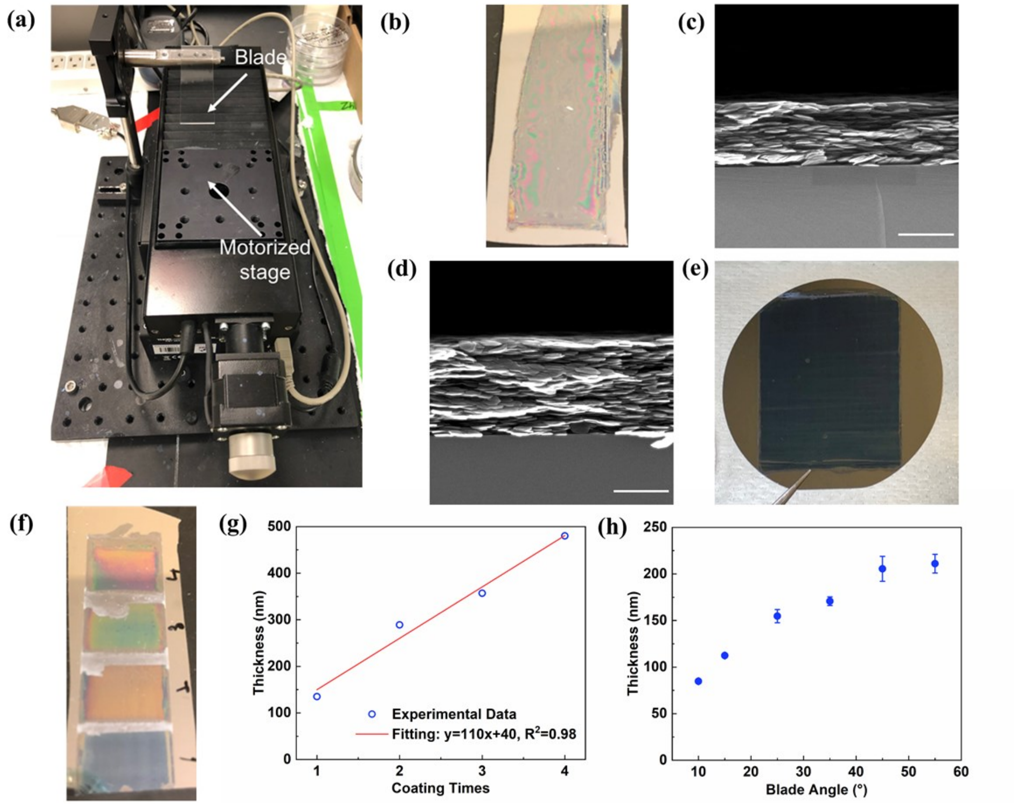

Figure S4. Photograph of (a) the lab-built flow coater, and flow-coated films from gibbsite (b) aqueous suspension and (e-f) water/ethanol mixture suspension. Typical cross-sectional SEM images taken at the (c) edge and (d) center of the film in (b) confirm thickness gradient along width of the film. All scale bars are 500 nm. The films in (f) from the bottom to top are deposited at 3mm/s for 1, 2, 3 and 4 times and their corresponding thickness is shown in (g). SEM images of the film deposited for 3 times are shown in Figure 2(c-d). (h) Dry film thickness h_d as a function of blade angle.

Spin Coating of Gibbsite NPTs

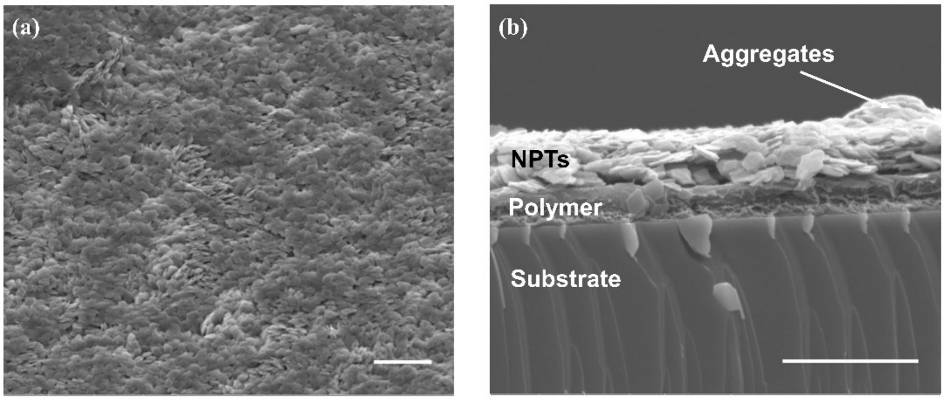

Figure S5. (a) Top-down and (b) cross-sectional SEM images of a spin-coated gibbsite NPT film using a 20 wt% gibbsite aqueous suspension. The features on the substrate were caused by fracture of the Si wafer for imaging. Aggregates of NPTs due to spin coating can also be observed. All scale bars are 2 µm.

GIWAXS Measurement of Larger NPT Packings

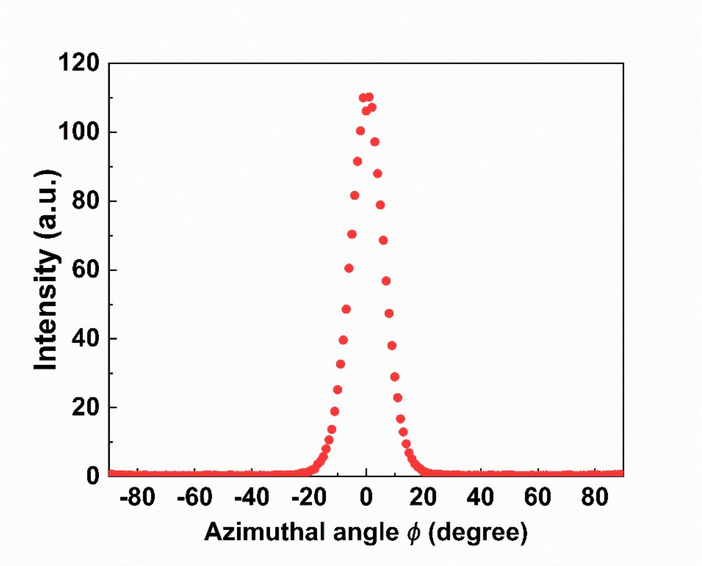

Figure S6. Azimuthal intensity profile across the (002) peak constructed from the GIWAXS pattern of a ~200 nm NPT film prepared with larger NPTs (one seeded-growth step). Herman's order parameter S_{GIWAXS} is calculated to be 0.95.

Ellipsometry Modelling of a Neat Gibbsite NPT Film

Three different models are used to understand the structure of the gibbsite NPT film: isotropic, uniaxial and biaxial models. One Cauchy dispersion relation is used in the isotropic model to obtain the refractive index (n) of the film, whereas two Cauchy relations are used in the uniaxial model to describe refractive index for the in-plane (n_o) and out-of-plane (n_e) directions of the film. The mean-square error (MSE) of the isotropic model (36.15) is significantly higher than the uniaxial model (5.24), indicating a strong anisotropy in the film. A biaxial model with three Cauchy relations, although further decreases MSE, shows that the difference between n_x and n_y is fairly small (~0.01). As shown in Figure S7, the uniaxial model can describe the data with high accuracy. We believe the biaxial model results in over-fitting and thus use uniaxial models for subsequent analyses of all the gibbsite NPT films.

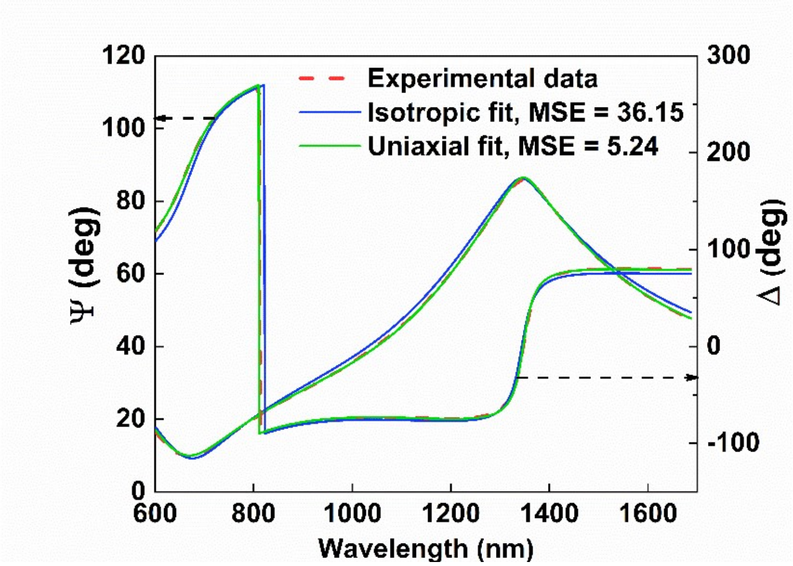

Figure S7. Ellipsometric angles ψ and Δ vs. wavelength for a ~300 nm gibbsite NPT film measured at 298 K. The blue and green lines show the fitting with an isotropic and uniaxial model, respectively.

Table S1 Thickness and refractive index of a neat gibbsite NPT film (Figure S7) determined from ellipsometry using isotropic, uniaxial and biaxial models

Model	Mean Square Error	Film Thickness (nm)	Refractive Index
Isotropic	36.15	304.99	$n = 1.446$
Uniaxial	5.24	303.79	$n_o = 1.470$; $n_e = 1.404$
Biaxial	4.43	304.49	$n_x = 1.469$; $n_y = 1.460$; $n_z = 1.400$

Determination of Packing Fraction based on Birefringence

The birefringence of a gibbsite NPT packing originates from both intrinsic birefringence and form birefringence due to the alignment of NPTs in a medium with a different refractive index.

Gibbsite has a monoclinic crystal structure with the following refractive index: $n_\alpha = n_\beta = 1.568$, $n_\gamma = 1.587$.[3] With it extinction angle making an angle of -21° with the z-axis (Figure S1), the intrinsic birefringence of a platelet is:[1]

$$\Delta n_i = (n_\gamma - n_\alpha) \times \cos 21° = 0.018 \tag{S1}$$

Then, the birefringence a gibbsite NPT packing due to intrinsic particle birefringence is determined by:

$$\Delta n_{intrinsic} = \Delta n_i \times \phi \times S = 0.017\phi \tag{S2}$$

Here, *S* is the order parameter of the packing which we calculate from GIWAXS ($S_{GIWAXS} = 0.96$). According to Wiener's model, the mean dielectric constant ε of a heterogeneous material consisting of subwavelength size particles dispersed in a medium can be related to the volume fraction ϕ of the particles according to equation (3):[4,5]

$$\varepsilon = \varepsilon_1 + \frac{\phi(\varepsilon_2 - \varepsilon_1)}{1 + (1 - \phi)\{(\varepsilon_2 - \varepsilon_1) / \varepsilon_1\}L} \tag{S3}$$

where ε_1 and ε_2 are the dielectric constant of the medium and particles, respectively, and *L* is the depolarization coefficient depending on the geometry of the particle. $L_\parallel$ and $L_\perp$ are depolarization coefficient parallel and perpendicular to the anisotropy axis (z-axis for gibbsite), respectively. They can be calculated as a function of ellipsoid aspect ratio according to reference 6. Gibbsite NPTs can be considered as high aspect oblate spheroids, resulting in $L_\parallel$ = 0.94, $L_\parallel$ = 0.03.[1,6] By substituting the values of *L* in equation (3), the refractive index and form birefringence of a heterogeneous material can be calculated as follows:[1,7]

$$n_{\parallel(\perp)} = \sqrt{\varepsilon_{\parallel(\perp)}} \tag{S4}$$

$$\Delta n_{form} = (n_\parallel - n_\perp) \times S \tag{S5}$$

Thus, the total birefringence of a gibbsite NPT packing can be obtained by summing up the two contributions:

$$\Delta n_{total} = \Delta n_{intrinsic} + \Delta n_{form} \tag{S6}$$

The volume fraction of NPTs in the neat gibbsite NPT films ($\varepsilon_1 = 1$) can be estimated based on Figure S8(a). The NPT films prepared with as-synthesized NPTs have a birefringence of -0.06, corresponding to a packing fraction of 0.84. When larger NPTs (after one seeded-growth step) are used, the birefringence decreases to -0.09 and the packing fraction decreases to 0.72 (Table S4). As shown in Figure S8(b), when the medium is polystyrene ($\varepsilon_1 = 1.588$), the birefringence turns positive, which agrees with experimental measurement (Table 1). The inversion of birefringence agrees with previous study on birefringence of nematic liquid crystal of gibbsite nanoplatelets in solvents with different refractive index.[1]

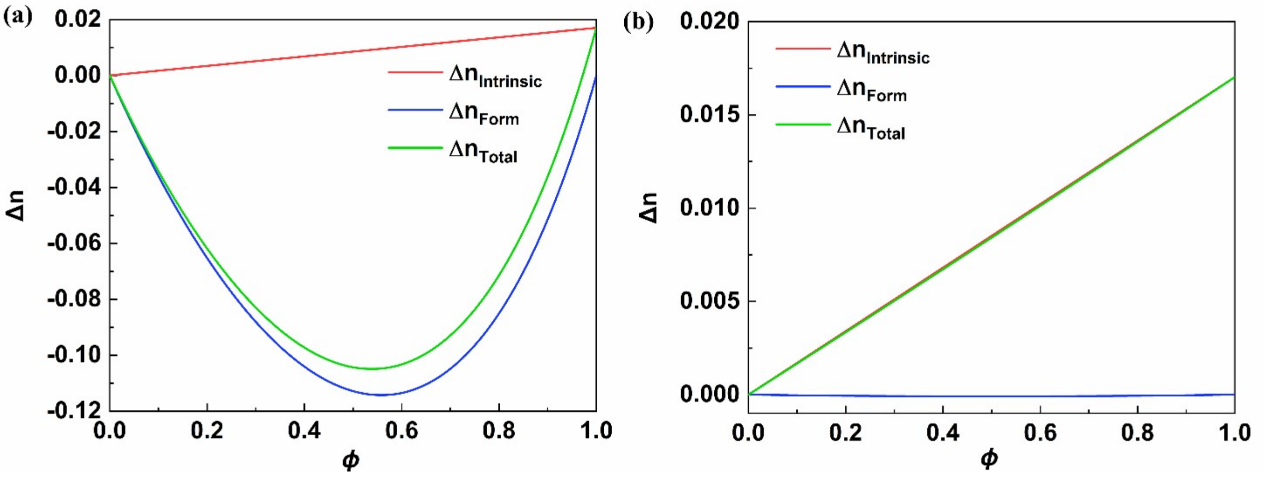

Figure S8. Calculated intrinsic, form and total birefringence of (a) neat gibbsite NPT films and (b) polystyrene-infiltrated NPT films as a function of volume fraction of NPTs.

Capillary Rise Infiltration of Polymer into Gibbsite NPT films

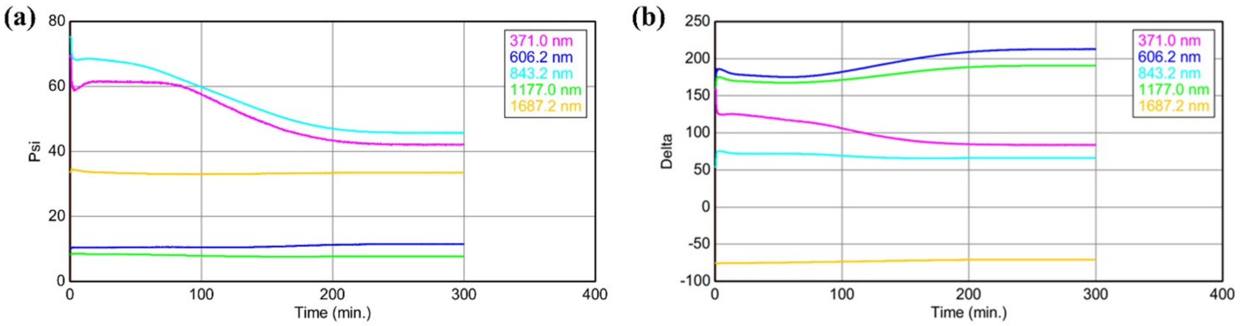

Figure S9. Raw (a) amplitude ratio (ψ) and (b) phase shift (Δ) data as a function of time, obtained using *in situ* spectroscopic ellipsometry while annealing a gibbsite NPT/PS-8k bilayer film at 403 K.

Estimation of Tortuosity in Gibbsite NPT Film

As shown in Figure 4, the composite layer thickness squared (l_{comp}^2) shows a linear dependence on time (t) in gibbsite NPT/PS-8k system at 423 K and the slope of the fitting represents the prefactor in the Lucas–Washburn model $\sigma R\cos\theta/4\tau^2\mu$. To compare with previous work on PS-8k infiltration into silica NP packings at 423 K, we assume the contact angle of polystyrene on silica and gibbsite is the same (20°) since both surfaces are rich in hydroxyl groups.[2,8] The mean pore radius is estimated to be 7 nm in gibbsite NPT stackings based on BET measurements.[9] According to our previous study, the viscosity of unentangled polymers in the interstices of weakly interacting nanoparticles can be increased by more than 2 orders of magnitude relative to the bulk viscosity.[8,10] For PS 8k, the viscosity at 423 K can be increased up to 8×10^3 Pa·s and we use this value as the upper limit of the viscosity of PS 8k in NPT packings. The parameters we use to infer the tortuosity in gibbsite NPT packings based on the Lucas−Washburn model are summarized in Table S2 and the tortuosity in gibbsite NPT packings is estimated to be >26, which is significantly higher than that in spherical packings (τ = 1.95).

Table S2 Parameters used for estimation of tortuosity in gibbsite NPT packings using the Lucas–Washburn model[8–12]

Nanoparticle/Polymer	**Surface tension as function of temperature,** $\sigma\ (T[°\mathrm{C}])(mN\ m^{-1})$	**Mean pore radius, R (nm)**	**Polymer Contact Angle, θ**	**Viscosity, μ (Pa·s)**	**Lucas-Washburn prefactor ($\frac{\sigma R\cos\theta}{4\tau^2\mu}$)**	**Tortuosity, τ**
Gibbsite NPT/PS-8k	40.5-0.068T	~7	20°	8×10^3 (upper limit)	9×10^{-18}	>26

Optical Transmittance of NPT Films by Flow Coating

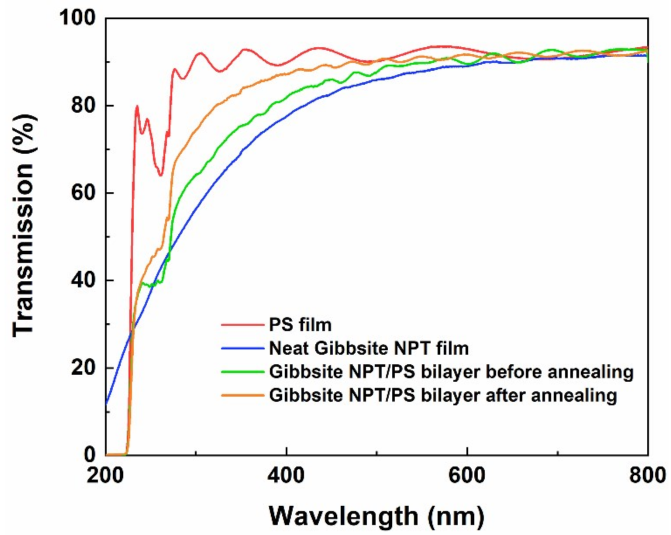

Figure S10. NIR-UV-vis spectra of neat PS (550 nm), neat gibbsite NPT (~2 um) and gibbsite NPT (~2 um)/PS (550 nm) films deposited on a quartz slide.

Platelet Fracture

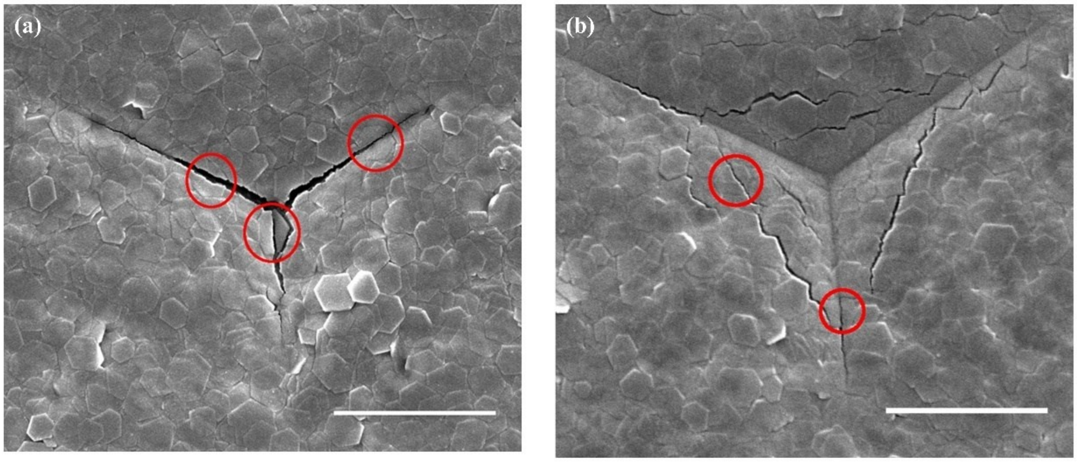

Figure S11. SEM images of indents on (a) an as-prepared NPT film and (b) a polymer-infiltrated NPT film. The contact depth for both indents was set to be 500 nm and the images were taken at a tilt angle of 40°. Red circles highlight fractured NPTs. Picture-frame cracks can be observed in (b). All scale bars are 1 µm.

Thermal Stability of Gibbsite NPT Films

For the gibbsite NPT film heated to 200°C, a small decrease in the film thickness (<5%) is observed starting at 100 °C as observed in Figure S12(a), likely due to the loss of adsorbed water.[2,13] A previous study based on XRD shows that although phase transformation of these NPTs starts to occur at 200 °C, the gibbsite phase remains the dominant phase.[9] When gibbsite NPT film is heated to 400 °C (Figure S12(b)), a large step loss in film thickness (~24%) is observed at around 230 °C, followed by a gradual loss in the film thickness. This trend agrees well with a previous thermogravimetric analysis of gibbsite and corresponds to the phase transformation of gibbsite to alumina.[2,9,13]

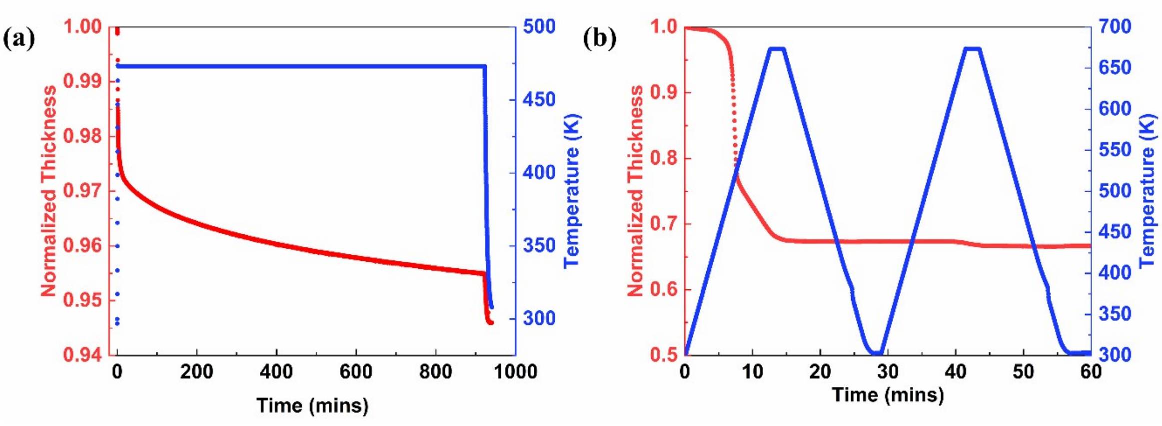

Figure S12. Thickness profile of (a) a 282 nm gibbsite NPT film annealed at 473K and (b) a 306 nm gibbsite NPT film annealed at 673K.

Table S3 Modulus and hardness of as-prepared, heat-treated, and polymer-infiltrated TiO_2 NP films

	Conditions	**Modulus (GPa)**	**Hardness (GPa)**
TiO_2 NPs (AR=1.9)	As prepared	16.29 ± 1.93	0.37 ± 0.10
	180 24hr	19.68 ± 3.33	0.60 ± 0.16
	After CaRI	28.63 ± 3.12	1.24 ± 0.20

Table S4 Particle Size, Packing Fraction, and Mechanical Properties of Gibbsite NPT (after one seeded growth step) films

	Size		Packing Fraction	Mechanical Properties		
	Diameter (nm)	**Thickness (nm)**		**Modulus (GPa)**	**Hardness (GPa)**	**Fracture Toughness ($MPa \cdot m^{1/2}$)**
Gibbsite NPTs (one seeded growth)	465 ± 64	18 ± 5	0.72	2.34 ± 0.41	0.07 ± 0.02	0.28 ± 0.03

Fracture of a Micropillar on an As-prepared NPT Film

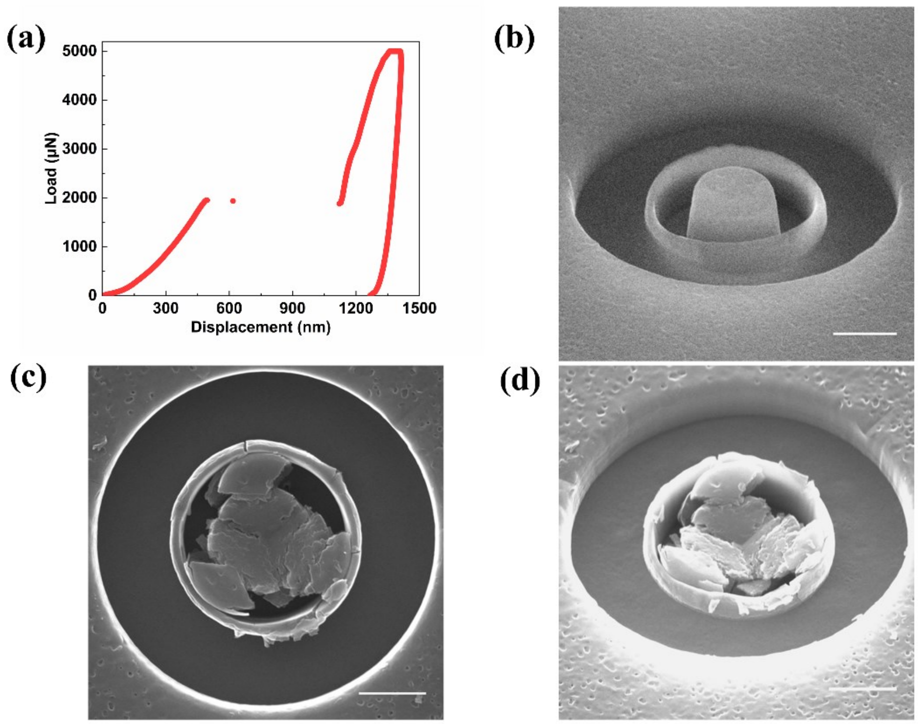

Figure S13. (a) Load-displacement curve from the pillar-splitting test of a micropillar on an as-prepared gibbsite NPT film. SEM images of the same pillar (b) before and (c-d) after the pillar-splitting test. All scale bars are 2 μm.

Scratch Test Load-displacement Set-up and Typical Curves

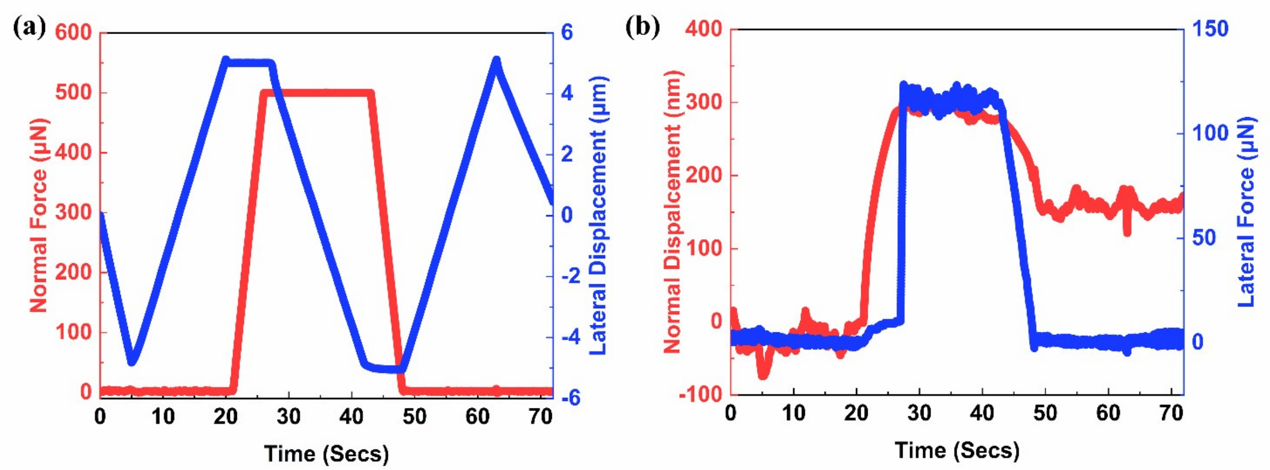

Figure S14. (a) Normal force and lateral displacement as a function of time set in scratch tests. (b) Typical normal displacement and lateral force recorded in a scratch test on a neat gibbsite NPT film.

Calculation of Normalized Lateral force

The lateral force on tip during the scratch test is a function of scratch depth and can be normalized by cross-sectional area of the grooved track (A in Figure 8(a)) for evaluation of scratch resistance. A can be calculated as:

$$A = \frac{1}{2} \times W \times d \tag{S7}$$

Where W is the width of the grooved track and d is the indented depth. For a Berkovich indenter with a face angle of 65.3°, W can be expressed as:[14]

$$W = 2\sqrt{3} \times d \times \tan 65.3° \tag{S8}$$

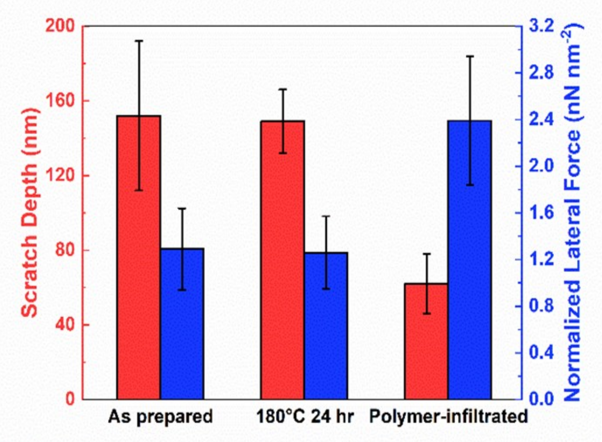

Figure S15. Final scratch depth and normalized lateral force of as-prepared, heat-treated (180°C 24 hr) and polymer-infiltrated TiO_2 NP films.

Reference:

1 A. A. Verhoeff, R. P. Brand and H. N. W. Lekkerkerker, *Mol. Phys.*, 2011, **109**, 1363–1371.
2 A. M. Wierenga, T. A. J. Lenstra and A. P. Philipse, *Colloids Surfaces A Physicochem. Eng. Asp.*, 1998, **134**, 359–371.
3 R. C. Shannon, B. Lafuente, R. D. Shannon, R. T. Downs and R. X. Fischer, *Am. Mineral.*, 2017, **102**, 1906–1914.
4 J. Kim, L. Martinelli, K. Lahlil, J. P. Boilot, T. Gacoin and J. Peretti, *Appl. Phys. Lett.*, 2014, **105**, 061102.
5 W. L. Bragg and A. B. Pippard, *Acta Crystallogr.*, 1953, **6**, 865–867.
6 J. A. Osborn, *Phys. Rev.*, 1945, **67**, 351.
7 R. Oldenbourg and T. Ruiz, *Biophys. J.*, 1989, **56**, 195–205.
8 J. L. Hor, H. Wang, Z. Fakhraai and D. Lee, *Soft Matter*, 2018, **14**, 2438–2446.
9 S. Louaer, Y. Wang and L. Guo, *ACS Appl. Mater. Interfaces*, 2013, **5**, 9648–9655.
10 J. L. Hor, H. Wang, Z. Fakhraai and D. Lee, *Macromolecules*, 2018, **51**, 5069–5078.
11 G. T. Dee and B. B. Sauer, *J. Colloid Interface Sci.*, 1992, **152**, 85–103.
12 S. Ralf, J. Karin and B. Ralf, *J. Phys. Condens. Matter*, 2001, **13**, 4915.

13 X. Zhang, P. L. Huestis, C. I. Pearce, J. Z. Hu, K. Page, L. M. Anovitz, A. B. Aleksandrov, M. P. Prange, S. Kerisit, M. E. Bowden, W. Cui, Z. Wang, N. R. Jaegers, T. R. Graham, M. Dembowski, H. W. Wang, J. Liu, A. T. N'Diaye, M. Bleuel, D. F. R. Mildner, T. M. Orlando, G. A. Kimmel, J. A. La Verne, S. B. Clark and K. M. Rosso, *ACS Appl. Nano Mater.*, 2018, **1**, 7115–7128.

14 C. T. Pan, T. T. Wu, C. F. Liu, C. Y. Su, W. J. Wang and J. C. Huang, *Mater. Sci. Eng. A*, 2010, **527**, 2342–2349.